

# Initial Decomposition of the Condensed-Phase $\beta$ -HMX under Shock Waves: Molecular Dynamics Simulations

Ni-Na Ge,<sup>†,‡</sup> Yong-Kai Wei,<sup>†,‡</sup> Guang-Fu Ji,<sup>\*,†</sup> Xiang-Rong Chen,<sup>\*,†,§</sup> Feng Zhao,<sup>†</sup> and Dong-Qing Wei<sup>\*,||</sup>

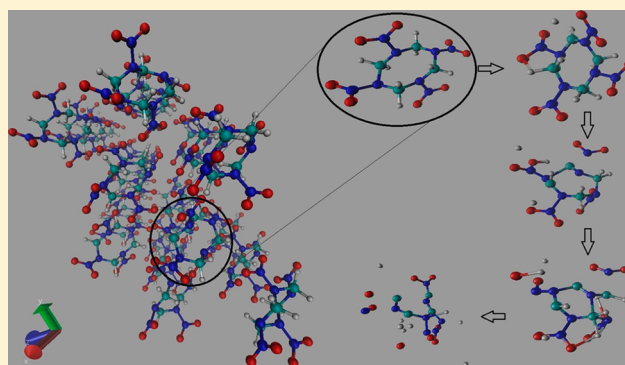
<sup>†</sup>National Key Laboratory of Shock Wave and Detonation Physics, Institute of Fluid Physics, Chinese Academy of Engineering Physics, Mianyang 621900, China

<sup>‡</sup>Institute of Computational Physics, Sichuan University, Chengdu 610064, China

<sup>§</sup>International Centre for Materials Physics, Chinese Academy of Sciences, Shenyang 110016, China

<sup>||</sup>State Key Laboratory of Explosion Science and Technology, Beijing Institute of Technology, Beijing 00081, China

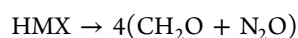
**ABSTRACT:** We have performed quantum-based multiscale simulations to study the initial chemical processes of condensed-phase octahydro-1,3,5,7-tetranitro-1,3,5,7-tetrazocine (HMX) under shock wave loading. A self-consistent charge density-functional tight-binding (SCC-DFTB) method was employed. The results show that the initial decomposition of shocked HMX is triggered by the N–NO<sub>2</sub> bond breaking under the low velocity impact (8 km/s). As the shock velocity increases (11 km/s), the homolytic cleavage of the N–NO<sub>2</sub> bond is suppressed under high pressure, the C–H bond dissociation becomes the primary pathway for HMX decomposition in its early stages. It is accompanied by a five-membered ring formation and hydrogen transfer from the CH<sub>2</sub> group to the –NO<sub>2</sub> group. Our simulations suggest that the initial chemical processes of shocked HMX are dependent on the impact velocity, which gain new insights into the initial decomposition mechanism of HMX upon shock loading at the atomistic level, and have important implications for understanding and development of energetic materials.



## 1. INTRODUCTION

The octahydro-1,3,5,7-tetranitro-1,3,5,7-tetrazocine (HMX) is an important energetic material, which was widely used as explosives and rocket propellants. But the decomposition mechanism of HMX remains unclear after centuries of use. Understanding the complex chemical processes is required to build an improved model for combustion or detonation.

Over the years, a lot of experimental studies have been made to investigate thermodynamic and mechanical properties of HMX.<sup>1–13</sup> Zaug<sup>1</sup> determined the elastic constants of the single HMX crystals through the ultrasonic sound speed measurements and impulsive stimulated light scattering (ISLS). Dick and Martinez<sup>2</sup> investigated the elastic precursor decay dependence on impact stress by the VISAR experiments. Marsh<sup>3</sup> presented the Hugoniot curves. Yoo and Cynn<sup>4</sup> reported studies of the chemical reactions of HMX under the hydrostatic and nonhydrostatic compression. To explore the possible decomposition production, Brill et al.<sup>5,6</sup> investigated the reaction pathways of HMX through the *T*-jump/FTIR spectroscopy techniques, which indicated two competing global reactions during the thermal decomposition of the condensed-phase HMX:



They suggested most reactive gases are dependent not only on the temperature but also on the pressure. Initially, the reaction products of HMX yield mainly N<sub>2</sub>O at low temperatures (298 °C) or NO<sub>2</sub> at higher temperatures (392 °C). Moreover, the global nitrogen and carbon schemes of NO<sub>2</sub> → NO → N<sub>2</sub> and CH<sub>2</sub>O → CO (CO<sub>2</sub>) shift to the right at higher pressure.

Moreover, Tang et al.<sup>7</sup> also explored the possible species during chemical reactions by the CO<sub>2</sub> laser assisted combustion techniques where H<sub>2</sub>O, CH<sub>2</sub>O, HCN, NO<sub>2</sub>, N<sub>2</sub>O, N<sub>2</sub>, CO, and NO were suggested. Pulham et al.<sup>8</sup> investigated the properties of solid-state structure HMX under extreme conditions during detonation; the limiting detonation velocity is 9.1 km/s and the detonation pressure is 39 GPa.

Recently, a few theoretical studies have been reported for the gas-phase HMX.<sup>14–17</sup> Zhang and Truong<sup>14,15</sup> and Lewis et al.<sup>16</sup> performed ab initio studies and find that N–NO<sub>2</sub> bond cleavage triggers the energetic material thermal decomposition of HMX. In addition, some theoretical studies have been reported the initial thermal decomposition step for gas-phase HMX dependent on the pressure and the temperature. For example, Zhang and Truong<sup>15</sup> found the HONO elimination channel is the dominant path at low

Received: September 13, 2012

Published: October 18, 2012

temperatures and in the temperature range 500–1500 K the  $\text{NO}_2$  fission channel is found to be dominant. Wang and Brower<sup>18</sup> suggested that the elimination of  $\text{HNO}_2$  or  $\text{HNO}$  played an important role at high pressure, because the homolytic cleavage of the  $\text{N}-\text{NO}_2$  bond was suppressed under high pressure.

The decomposition path for the condensed-phase HMX also drew much attention as well. Sharia and Kuklja<sup>17,19,20</sup> performed a combined study based on density functional theory calculations coupled with the conventional transition-state theory (CTST) and variational transition-state theory (VTST), and a microscale materials morphology description to analyze the effect of the surface interfaces, voids, molecular vacancies (defects), or crystalline field on the interplay of main decomposition reactions in HMX. Glascoe et al.,<sup>21</sup> Henson et al.,<sup>22</sup> and Brill and Karpowicz<sup>23</sup> found that HMX experiences a polymorphic transition, from the  $\beta$  to the  $\delta$  phase during the thermal decomposition. In 2002, the electronic structure and density of states of the crystalline HMX were investigated at DFT-B3LYP/6-31G\*\* level by Ji et al.<sup>24</sup> From the bonding orders and the population analysis, they found that the bonds of  $\text{N}-\text{NO}_2$  are the weakest, which could trigger explosion. Prasad et al.,<sup>25</sup> Suryanarayana et al.,<sup>26</sup> McGuire and Tarver<sup>27</sup> suggested that the  $\text{C}-\text{N}$  bond scission plays an important role in the decomposition reaction for the condensed phase, where the  $\text{C}-\text{N}$  bond scission mechanism was energetically favored and the steric constraints disfavored  $\text{N}-\text{NO}_2$  bond dissociation. In addition, Zhu et al.<sup>28</sup> identified the initial chemical processes behind shock fronts using ab initio MD combined with MSST, which indicated the initial decomposition of the shocked HMX was triggered by the  $\text{N}-\text{O}$  bond breaking and the ring-opening under the impact speed 6.5 km/s. Cui et al.<sup>29</sup> investigated the electronic structures and the mechanical and thermodynamic properties of solid HMX using the DFT-GGA method. They found that  $\text{N}-\text{NO}_2$  and  $\text{C}-\text{N}$  were easily compressed with increasing pressure and became relatively strong and stable. In contrast, the  $\text{C}-\text{H}$  bond became weaker under high pressure, which is supported by some other theoretical studies.<sup>30</sup>

Theoretical studies of HMX have made significant progress due to the availability of the simulation methods developed in recent years. However, the chemical processes upon dynamical loading, such as shock waves are rare to see. In this work, we made simulations of shock-induced chemistry in HMX using the MD in conjunction with multiscale shock technique (MSST) in the CP2K software package.<sup>31</sup> A self-consistent charge density-functional tight-binding (SCC-DFTB) method was adapted. The question that our studies try to answer is how shock waves trigger chemical reactions.

## 2. COMPUTATIONAL DETAILS

The MD in conjunction with multiscale shock technique (MSST) is a simulation method based on the Navier–Stokes equations for compressible flow.<sup>32</sup> The computational cell of the multiscale technique follows a Lagrangian point through the shock wave, which could be simulated with fewer atoms and lower computational cost.<sup>33</sup> The multiscale shock technique simulates steady shock waves (that is, constant shock speed) by the time-evolving equations of motion for atoms and volume of the computational cell to constrain the shock-propagation-direction stress to the Rayleigh line and energy to the Hugoniot relation. For a specified shock speed, the Hugoniot relation  $E - E_0 = 1/2(P + P_0)(V_0 - V)$  could be obtained by the conservation of mass, momentum, and energy across the shock front,<sup>34a</sup> where  $E$  is the energy,  $P$  is the negative of the diagonal

component of the stress tensor in the direction of the shock, and  $V$  is the volume. A subscript 0 refers to the preshocked state, whereas quantities without subscripts refer to the postshocked state. The thermodynamic path connecting the initial state of the system to its final (Hugoniot) state could be described by the Rayleigh line  $P - P_0 = U^2\rho_0(1 - \rho_0/\rho)$  (where  $U$  is the shock velocity and  $\rho$  is the density).<sup>34a</sup> These two relations describe a steady planar shock wave within continuum theory, which have to be obeyed for steady shock waves.

Indeed, the molecular dynamics simulation techniques based on the first principle quantum mechanics,<sup>35,36</sup> along with the multiscale shock technique (MSST) could help us understand, in molecular details, the reactive front of energetic materials under shock loading. This technique has been employed for simulating the shocked nitromethane by Reed et al.,<sup>34b</sup> the shock-induced phase transformation of graphite to diamond by Mundy et al.,<sup>36</sup> the reactivity of shocked insensitive explosive triaminotrobenzene by the Manaa et al.,<sup>37</sup> and the equation of state and kinetics of shocked water by the Goldman et al.<sup>34a</sup> These indicate that the computational methods have been very useful in studying chemical processes of the materials at extreme conditions.

Our electronic-structure calculations are based on the self-consistent charge density-functional tight binding (SCC-DFTB) scheme.<sup>38</sup> This is based on a second-order expansion of the Kohn–Sham total energy in density-functional theory (DFT) with respect to charge density fluctuations. This method allows for description of total energies, atomic forces, and charge transfer in a self-consistent manner. It has been successfully tested on organic and bioorganic systems<sup>39,40</sup> and has been shown to accurately predict reaction energies.<sup>41–43</sup> This method was applied to the study of nitromethane and TATB under pressure<sup>37,42</sup> which has yielded results comparable to those obtained from the other density functional calculations. Furthermore, it is also applied to study the reactivity of shocked perfect crystal TATB.<sup>37</sup>

We perform simulations of the following shock velocities (km/s): 8, 10, and 11, which is near the experimentally measured steady detonation shock speed.<sup>8</sup> This simulation supercell consists of a  $3 \times 2 \times 2$  conventional unit cell with 24 HMX molecules (672 atoms) whose initial positions were taken from the experimentally determined X-ray crystal structure.<sup>44</sup> During the structure optimization, the conjugate gradient was used for the geometry optimization. The convergence criterion for the maximum geometry change between the current and the last optimizer iteration was converged to less than  $3.0 \times 10^{-3}$  bohr. The convergence criterion for the maximum force component of the current configuration was converged to less than  $4.5 \times 10^{-4}$  hartree/bohr. The convergence criterion for the root-mean-square (RMS) geometry change between the current and the last optimizer iteration was converged to less than  $1.5 \times 10^{-3}$  bohr. The convergence criterion for the root-mean-square (RMS) force of the current configuration was converged to less than  $3.0 \times 10^{-4}$  hartree/bohr, respectively. The wave function was converged to less than  $10^{-6}$  au. The initial temperature and pressure were set as 300 K and 0 GPa, respectively. And the initial velocities were randomly chosen. Uniaxial compression of the shock wave occurred along the  $a$  lattice vector. For the shock compression simulations, the fictitious cell mass was set to  $5.0 \times 10^{10}$  au. The wave function convergence criteria was  $10^{-6}$  au, for the shock speeds 8 km/s, the time step was 0.1 fs for up to 80 ps, and then for the shock speeds of 10 and 11 km/s, the time step was 0.05 fs.

To follow the chemical processes as the shock wave propagates through HMX, we implemented a procedure to identify individual molecules based on bond-length and lifetime criteria in the simulation. This method is also used in the previous literature.<sup>37</sup> The configurations were drawn from the trajectory file: When two atoms are closer than a given cutoff distance  $r_c$  for a time greater than 100 fs, they belong to the same molecule.

The calculated equilibrium lattice constants of the unit-cell HMX are shown in Table 1. The results of our calculations are

**Table 1. Calculated at 0 GPa and 300 K Lattice Constants of  $\beta$ -HMX Compared with the Theoretical and Experimental Data**

|                   | $a$ (Å) | $b$ (Å) | $c$ (Å) | $\alpha$ (deg) | $\beta$ (deg) | $\gamma$ (deg) |
|-------------------|---------|---------|---------|----------------|---------------|----------------|
| exp <sup>45</sup> | 6.54    | 11.05   | 8.70    | 90             | 124.3         | 90             |
| exp <sup>46</sup> | 6.54    | 11.05   | 8.702   | 90             | 124.325       | 90             |
| ref 17            | 6.72    | 11.41   | 8.91    | 90             | 124.06        | 90             |
| ref 47            | 6.52    | 10.99   | 8.62    | 90             | 122.73        | 90             |
| ref 48            | 6.70    | 11.35   | 8.91    | 90             | 124.13        | 90             |
| ref 49            | 6.58    | 11.12   | 8.76    | 90             | 124.30        | 90             |
| this work         | 6.54    | 11.05   | 8.70    | 90             | 123.02        | 90             |

in agreement with the experimental structures of Choi and Boutin,<sup>45</sup> as well as the results of Eiland and Pepinsky.<sup>46</sup> Other theoretical results<sup>17,47–49</sup> are also presented for comparison. We also find our calculations are in even better agreement with experimental data. For the larger  $3 \times 2 \times 2$  supercell with 24 HMX molecules (672 atoms), the calculated energy–volume plot is shown in Figure 1. We can then acquire the most stable

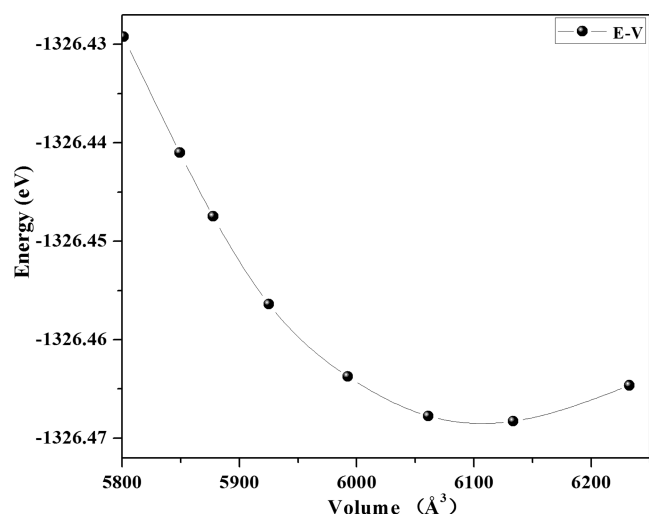


**Figure 1.** Calculated energy as a function of cell volume.

structure (lowest energy) with the lattice parameters,  $a = 18.638$  Å,  $b = 21.834$  Å,  $c = 16.967$  Å and  $\alpha = 90.00^\circ$ ,  $\beta = 123.02^\circ$ ,  $\delta = 90.00^\circ$ .

Figure 2 shows the pressure dependence of HMX on volume under shock compression using the multiscale scheme with the DFTB method. For HMX, Olinger et al.<sup>50</sup> Yoo and Cynn,<sup>51</sup> Marsh,<sup>3</sup> and Gump and Peiris<sup>52</sup> have measured the experimental shock Hugoniot curve. Our calculation agrees well with the nonhydrostatic and the shock Hugoniot, at least to 30 GPa. The data above 30 GPa show a small difference between our simulations and experiments because exothermal reactions in our simulations might be different from the experimental situation. In addition, their

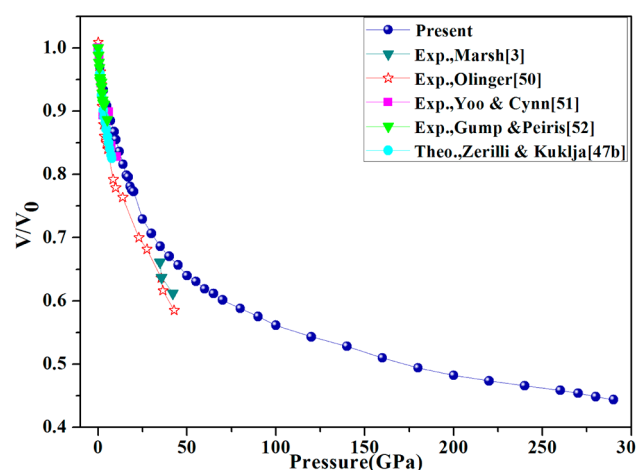


**Figure 2.** Volume dependence of HMX on pressure.

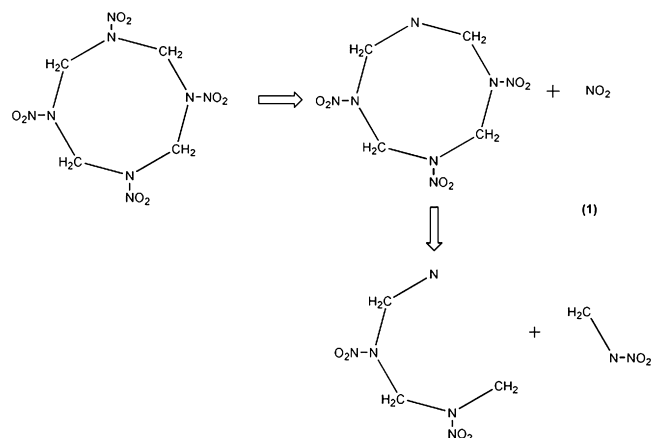
studies did not consider the factors of temperature. Further, the calculated pressure is also compared with the theoretical 300 K isotherm from the first principles by Zerilli and Kuklja.<sup>47b</sup>

### 3. RESULTS AND DISCUSSION

#### 3.1. Initial Reaction Kinetics of HMX under Impact Loading.

In the previous theoretical studies, the possible decomposition reaction pathways of HMX in the gas phase were (1) N–NO<sub>2</sub> bond dissociation, (2) HONO elimination, (3) C–N bond scission of the ring, and (4) the concerted ring fission. In this paper, we find that the decomposition pathway of HMX in condensed phase is dependent on the shock wave velocity. The N–NO<sub>2</sub> bond dissociation is the primary pathway for HMX decomposition in its early stages at low velocity impact (8 km/s). Then, at the high velocity impacts (10 and 11 km/s), the C–H bond dissociation is the primary pathway for HMX decomposition in its early stages.

**3.1.1. Initial Decomposition Step at Low Velocity Impact (8 km/s).** During the initial shock compression of condensed-phase HMX under 8 km/s shock wave, the first vibrations of the nitro group caused a distortion in HMX. At 1.63 ps, the N–N bond broke and formed NO<sub>2</sub>. Afterward, the HMX ring was opened through the C–N bond scission, forming a long radical chain. As the simulation continued, the long radical chain decomposed into two short ones, as shown in eq 1.



At this low velocity impact, our results show dominance of NO<sub>2</sub> fission in the early stages of decomposition due to lower activation barrier and larger pre-exponential factor (i.e., larger activation



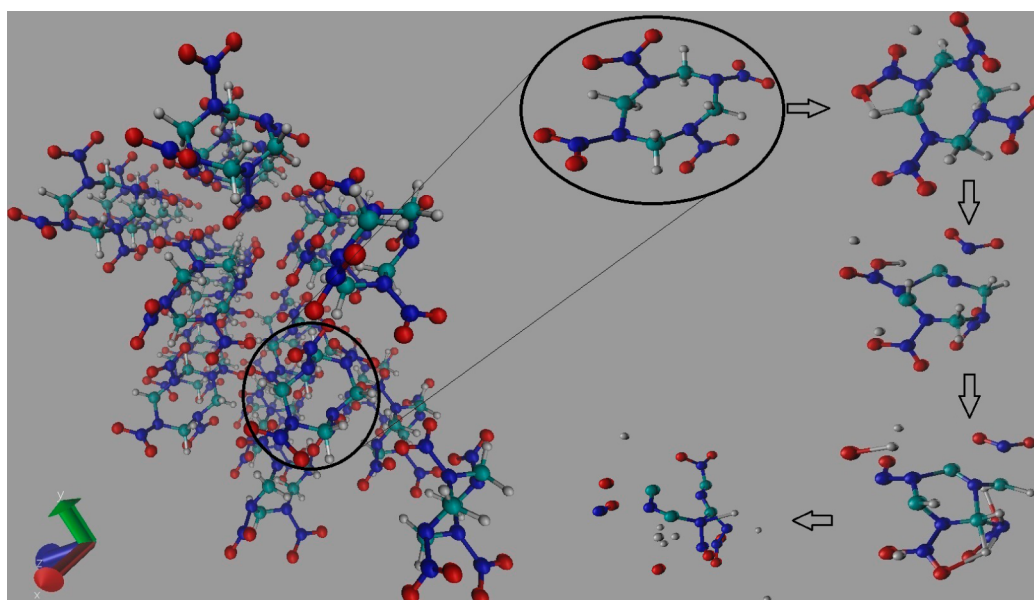


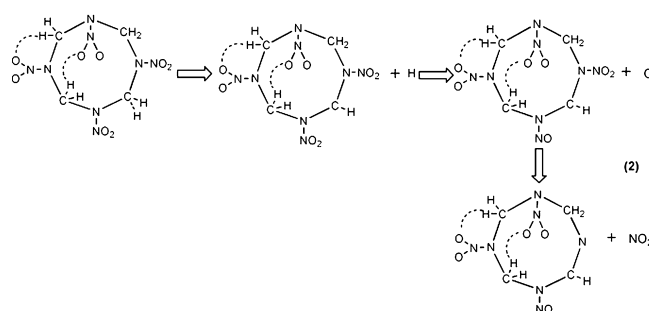
**Figure 3.** Bond rupture sequence observed in a  $3 \times 2 \times 2$  supercell for HMX under high impact loading ( $V_{\text{imp}} = 11$  km/s). Color code: white, hydrogen; red, oxygen; blue, nitrogen; green, carbon. (a) Tt 2.61 ps, C–H bond fracture accompanied by H ion transfer. (b) At 2.64 ps, N–NO<sub>2</sub> bond cleavage. (c) At 3.0 ps, N–O bond cleavage. (d) At 3.1 ps, C–N bond cleavage.

entropy) for the NO<sub>2</sub> rate constant,<sup>53</sup> which completely agree with experimental and theoretical studies.<sup>16,18,54–56</sup>

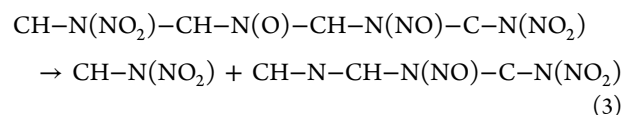
At 4.55 ps, two unstable radicals  $(\text{CH}_2\text{NNO}_2)_2\text{CH}_2\text{--N}$  and  $\text{CH}_2\text{--N}(\text{NO}_2)$  recombined to form  $(\text{CH}_2\text{NNO}_2)_3\text{CH}_2\text{--N}$ . The unstable radical  $(\text{CH}_2\text{NNO}_2)_3\text{CH}_2\text{--N}$  decomposed into  $\text{CH}_2\text{--N}(\text{CH}_2\text{NNO}_2)_2\text{CH}_2\text{--N}(\text{NO})$  and O radicals. Then the fragment NO<sub>2</sub> recombined with the O radical and formed NO<sub>3</sub> at 4.87 ps, which was also observed in the thermal decomposition of HMX.<sup>53</sup> As the simulation continued, the radical  $\text{CH}_2\text{--N}(\text{CH}_2\text{NNO}_2)_2\text{CH}_2\text{--N}(\text{NO})$  further decomposed into  $(\text{CH}_2\text{N})_2\text{CH}_2\text{--N}(\text{NO}_2)\text{CH}_2\text{--N}(\text{NO})$  and NO<sub>2</sub>. In summary, HMX does not completely decompose due to the low velocity impact, and NO<sub>2</sub> is the major reaction product under the low velocity impact 8 km/s.

**3.1.2. Initial Decomposition Step under High Impact Velocity (10 and 11 km/s).** As the impact velocity increased, the initial decomposition of HMX became quite different. During the initial shock compression, the initial decomposition pathway for HMX was triggered by C–H bond breaking. At the same time, a five-membered ring was formed and hydrogen transferred from the CH<sub>2</sub> group to the –NO<sub>2</sub> group. Then the N–N bond broke and formed NO<sub>2</sub>. As the simulation continued, the N–O bond broke, and the ring opened, forming many small pieces in the end. The order of the bond cleavage during the decomposition is shown in Figure 3.

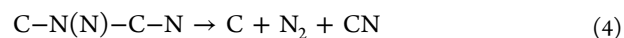
Actually, different HMX molecules experienced various reaction paths under shock loading. To make specific analysis of the decomposition processes, we selected four typical HMX molecules for detailed investigation. It exhibited four distinct decomposition stages after shockwave impact. As for the first HMX molecule, its nitro group vibrated strongly under strong impact. At 2.57 ps, one C–H bond broke and produced a H. At the same time, two five-membered rings were formed. At 2.58 ps, one N–O bond broke and produced an O. Then, one N–N bond broke and yielded NO<sub>2</sub>, which are shown in the eq 2.



Then the NO<sub>2</sub> decomposed into O and NO. At the same time, many C–H bonds were broken, producing many H. Some of the H were captured by O and formed fragments O–H that were considered as a major decomposition product in the shock decomposition of all energetic material. These were also considered as the basis for formation of water molecules. At 3.05 ps, the HMX ring was opened through the C–N bond scission and formed a radical chain  $\text{CH--N}(\text{HONO})\text{CH--N}(\text{O})\text{--CH--N}(\text{NO})\text{--C--N}(\text{NO}_2)$ . Then the H–O bond of the long chain was unstable and broken. At 3.08 ps, the long radical chain decomposed into two short radical chains, as shown in eq 3.



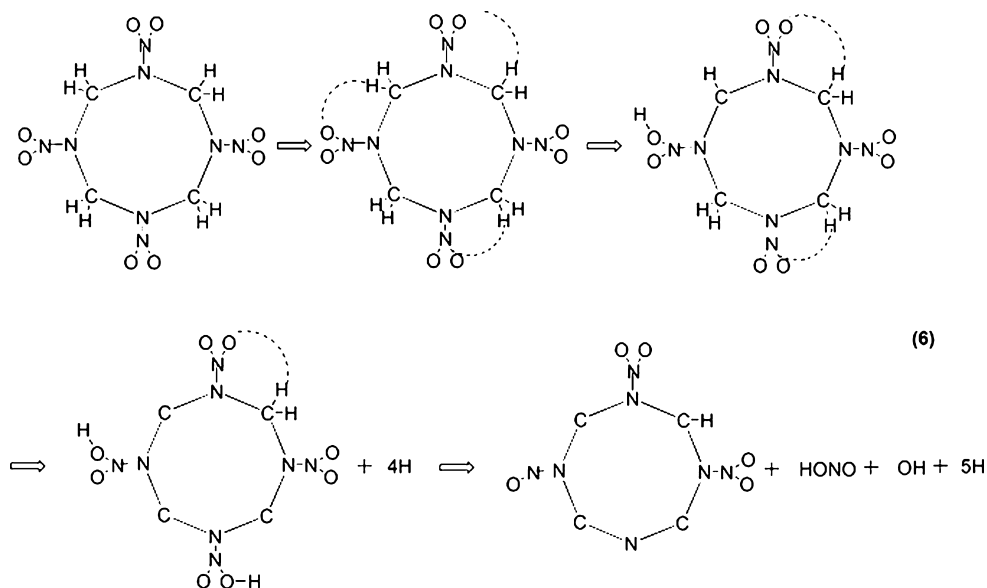
As the simulation continued, the stable intermediates (such as NO<sub>2</sub> and the transition state (TS) C–N(N)–C–N) were formed through N–NO<sub>2</sub> and C–H bond breaking. With increasing temperature and pressure, the C–N(N)–C–N chain further decomposed through eq 4; then the free oxygen and carbon atoms combined to generate the carbon monoxide (eq 5)



It is worth noting that the fragments  $\text{NO}_2$ ,  $\text{N}_2$ , and  $\text{CO}$  were considered major decomposition products in the reaction processes of all the energetic materials, which agrees with the proposed mechanism.<sup>16,57,58</sup>

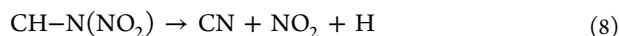
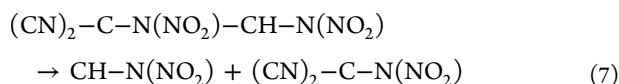
As for the second HMX molecule, at 2.36 ps, there were three five-membered rings. At 2.44 ps, there was a

hydrogen transferred from the  $\text{CH}_2$  group to the O of the  $\text{NO}_2$  group. At the same time, the C–H bond broke and produced many H ions. One H was captured by O to form an O–H radical. At 3.0 ps, the N–N bond and N–OH bond broke and formed HONO and OH, as shown in eq 6.



The unstable fragment HONO further decomposed to NO and OH through the N–O bond scission. At the same time,  $\text{C}-\text{N}(\text{NO}_2)-\text{CH}-\text{N}(\text{NO}_2)-\text{C}-\text{N}(\text{NO})-\text{C}-\text{N}$  was unstable and further decomposed into NO. At 3.18 ps, the ring was opened through the C–N bond scission.

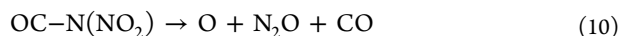
At 3.19 ps, one long radical chain decomposed into two short radical chains. Then the unstable fragment chain  $\text{CH}-\text{N}(\text{NO}_2)$  decomposed into CN,  $\text{NO}_2$ , and H, as shown in eqs 7 and 8.



The other long radical chain  $(\text{CN})_2-\text{C}-\text{N}(\text{NO}_2)$  was decomposed by the C–N scission



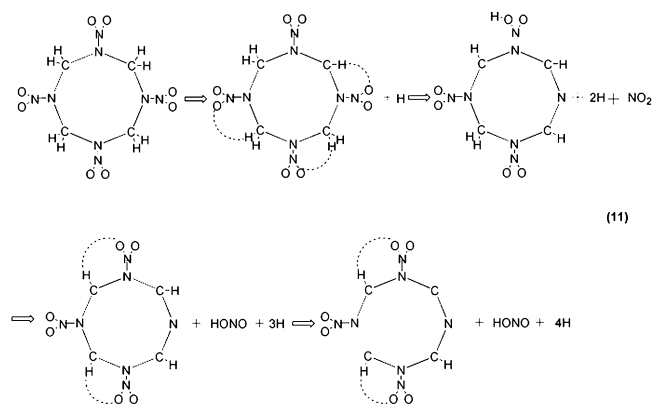
Then the  $\text{C}-\text{N}(\text{NO}_2)$  recombined with the O radical to produce  $\text{OC}-\text{N}(\text{NO}_2)$ . In the end,  $\text{OC}-\text{N}(\text{NO}_2)$  was decomposed by C–N and N–O bond scission.



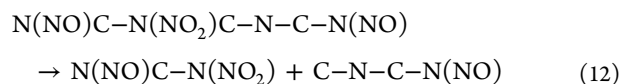
It is worth noting that the fragments  $\text{N}_2\text{O}$  and  $\text{CO}$  are considered major decomposition products in the reaction process of all energetic materials, Tang et al.<sup>7</sup> found that both  $\text{N}_2\text{O}$  and  $\text{CO}$  are the major species in the experiment, which also agrees with the mechanism proposed by the theoretical results.<sup>16,18,58–60</sup>

As for the third HMX molecule, there were three five-membered rings. The C–H bond broke and yielded a H at 2.52 ps. At 2.64 ps, the hydrogen transferred from the  $\text{CH}_2$  group to the O of the  $-\text{NO}_2$  group. At the same time, the N–N bond broke and produced a  $\text{NO}_2$  molecule. Then  $\text{NO}_2$  combined

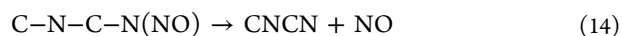
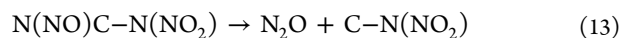
with free the H atom to generate HONO, and the ring was also opened through C–N bond scission (eq 11).



At 3.04 ps, the C–H and N–O bond fractured, resulting in a large number of H and O ions, respectively. At 3.21 ps, the long radical chain decomposed two short radicals by eq 12.



Then  $\text{N}(\text{NO})\text{C}-\text{N}(\text{NO}_2)$  and  $\text{C}-\text{N}-\text{C}-\text{N}(\text{NO})$  decomposed, respectively.

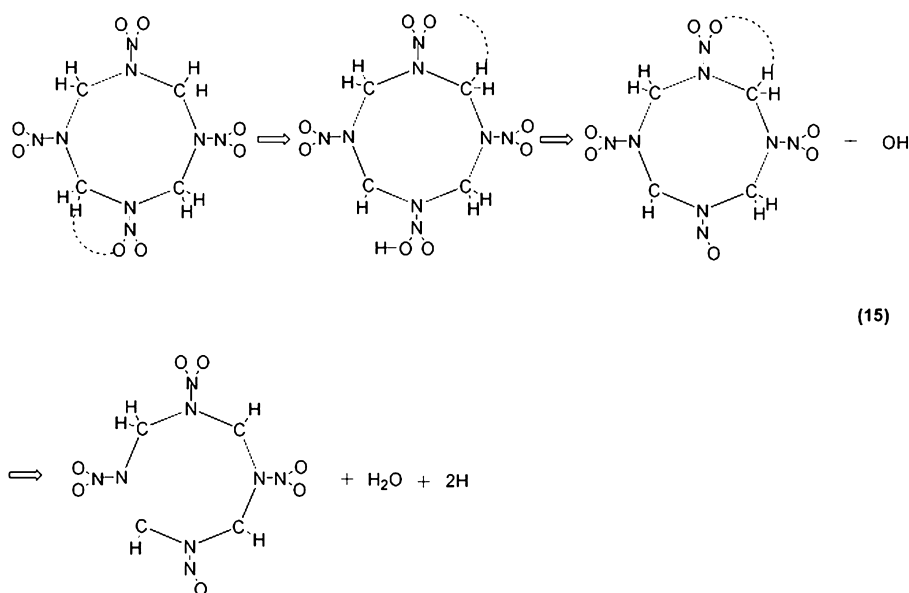


The final products were NO and CNCN, which are observed during the thermal decomposition of common energetic materials.<sup>7,61</sup> Furthermore, there are some other theoretical articles about NO and CNCN.<sup>18,28,53,58,59</sup> When the reactions

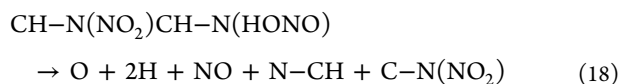
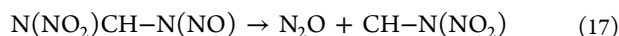
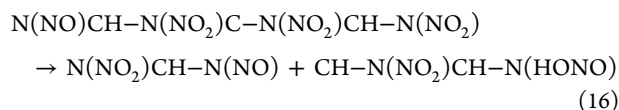
progressed, we saw that the gas NO not only was generated from the precursor gas NO<sub>2</sub> but also could be directly produced in the reaction shown in eq 14. This is consistent with previous observation that NO<sub>2</sub> is not a precursor for NO under explosion.<sup>62,63</sup>

As for the fourth HMX molecule, at 2.54 ps, one five-membered ring formed. Then one C–H bond broke and

produced H. Then there was a hydrogen transferred from the CH<sub>2</sub> group to the O of the NO<sub>2</sub> group. Afterward, the N–NOOH bond broke to generate HONO. At the same time, there is another five-membered ring formed. At 2.76 ps, the OH radical combined with one H and generated H<sub>2</sub>O. At the same time, the ring was opened though C–N bond scission, as shown in eq 15.



At 3.41 ps, the long radical chain decomposed to N(NO<sub>2</sub>)CH–N(NO) and CH–N(NO<sub>2</sub>)CH–N(NO<sub>2</sub>) radicals through eqs 16–18.



In the end of the simulation, we found the most dominant products were NO and N<sub>2</sub>. N<sub>2</sub>O and NO<sub>2</sub> would further decompose at high temperature and pressure as follows



The final stable molecules were N<sub>2</sub>, NO, and CO. It is consistent with the FTIR experiment,<sup>18</sup> where the final gas products contain CO and NO.

**3.2. Species Analysis under Impact Loading Conditions.** In Figure 4, we show the time evolution of the population of various key fragments (H<sub>2</sub>, O<sub>2</sub>, N<sub>2</sub>, H<sub>2</sub>O, N<sub>2</sub>O, NO, NO<sub>2</sub>, CO, and CO<sub>2</sub>) from  $V_{\text{imp}} = 8$  to 11 km/s. For  $V_{\text{imp}} = 8$  km/s, there were little chemical reactions, only ~3 NO<sub>2</sub>, ~1 N<sub>2</sub>O, and ~1 NO were formed during the course of simulation. Pulham et al.<sup>8</sup> reported the limiting detonation velocity as 9.1 km/s for HMX. In our simulation, there were a small number of chemical reactions under the 8 km/s impact velocity, which was shown in Figure 4a. For RDX, Strachan

et al.<sup>64</sup> reported that NO<sub>2</sub> was the only product in weak shock. In addition, Brill et al.<sup>5</sup> reported that the NO<sub>2</sub> were observed in the experiment. It is clear that our simulation results under the 8 km/s impact velocity is consistent with the previous theoretical and experimental results.

Compared with  $V_{\text{imp}} = 8$  km/s, the decomposition process had a significantly enhancement in  $V_{\text{imp}} = 10$  km/s. Figure 4b shows the time evolution of the population of key molecules at the  $V_{\text{imp}} = 10$  km/s, which HMX further decomposed. During the early stage (up to ~5 ps), N<sub>2</sub>, NO<sub>2</sub>, and NO increased significantly with the increasing time. After ~7 ps, the number of the NO, N<sub>2</sub>O, and H<sub>2</sub>O decreased with increasing time. During the expansion stage (after ~10 ps), the reaction products of the N<sub>2</sub>, CO<sub>2</sub>, and CO reached a final balance. Compared with the products at the  $V_{\text{imp}} = 8$  km/s, it is worth noting that there are some new reaction products at 10 km/s, such as H<sub>2</sub>O, CO, and CO<sub>2</sub> which are common reaction products in the previously theoretical simulation and experimental studies.

At  $V_{\text{imp}} = 11$  km/s impact velocity, there were larger quantities of CO (~50), N<sub>2</sub> (~33), and CO<sub>2</sub> (~15) in the expansion stage. The number of NO increased (~32) significantly and decreased (~10) in the expansion stage. Most notably, the N<sub>2</sub>O, H<sub>2</sub>O, and NO<sub>2</sub> fragments increased significantly. As the impact velocity increases, we found the significant reaction intermediate at very early stage was not NO<sub>2</sub>, which was said to result from N–NO<sub>2</sub> and C–N bond breakage in the thermolysis of RDX and HMX.<sup>25–27</sup> So, we think that the initial step of decomposition was not the homolysis of the N–NO<sub>2</sub> bond under strong shock compression. Our result was in agreement with the experiments<sup>5</sup> and theoretical results<sup>15,16,18,65</sup> that the homolytic cleavage of the N–NO<sub>2</sub> bond was suppressed under high pressure. Together with the result by Strachan et al.,<sup>64</sup> which indicate NO<sub>2</sub> is the main intermediates for low-velocity

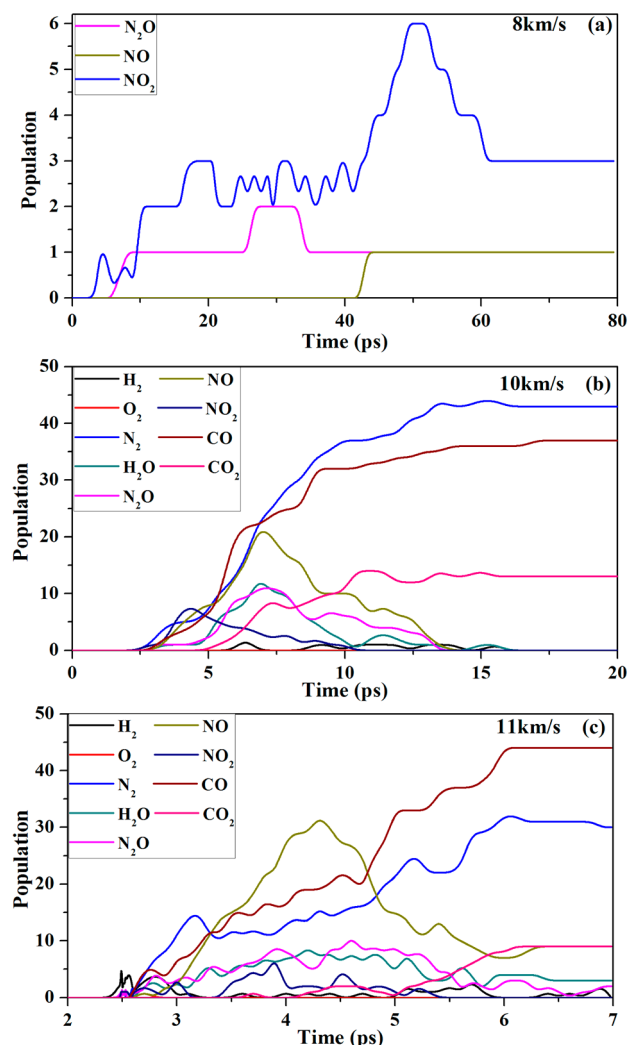


**Figure 4.** Decomposition products of solid-phase HMX under the various impact velocities: (a) 8 km/s; (b) 10 km/s; (c) 11 km/s.

shocks. At  $V_{\text{imp}} = 11$  km/s impact velocity, we found the product was  $\text{H}_2$  during the initial step, which indicated that C–H bond breaking was quite dominant in the early chemical reaction. Comparing with the case of nitromethane under the high pressure,<sup>34b</sup> Margetis and Kaxiras<sup>42</sup> found that sufficient uniform or uniaxial compression caused the C–H bond to be highly stretched before any significant bending of the nitro group occurs. Mana et al.<sup>66</sup> reported a caging effect plays a dominant role in promoting enhanced vibrations in C–H mode for the condensed-phase HMX, which eventually leads to a proton extraction.

During the detonation, the shockwave passed through the material and generated high pressures and temperatures. By summarizing our current and other previous work,<sup>5,18</sup> we found that the decomposition pathway of nitramines and nitrosamines was dependent on the shock velocity, which is closely related to the pressure and temperature of system upon shock loading. At  $V_{\text{imp}} = 8$  km/s, the most reactive gases were the  $\text{NO}_2$ ,  $\text{N}_2\text{O}$ , and  $\text{NO}$ . At  $V_{\text{imp}} = 10$  km/s, the  $\text{N}_2$ ,  $\text{CO}$ , and  $\text{CO}_2$  gases dominated; however, the numbers of the  $\text{NO}$ ,  $\text{N}_2\text{O}$ , and  $\text{H}_2\text{O}$  had an evidence decrease in the time scale of the detonation. When the impact velocity increased to 11 km/s, the  $\text{N}_2$ ,  $\text{CO}$ , and  $\text{CO}_2$  reached to a greater extent with the  $\text{NO}$  decreasing. Hence, the global nitrogen and carbon schemes of  $\text{NO}_2 \rightarrow \text{NO} \rightarrow \text{N}_2$  and  $\text{CO} (\text{CO}_2)$  was the final steady production pathway

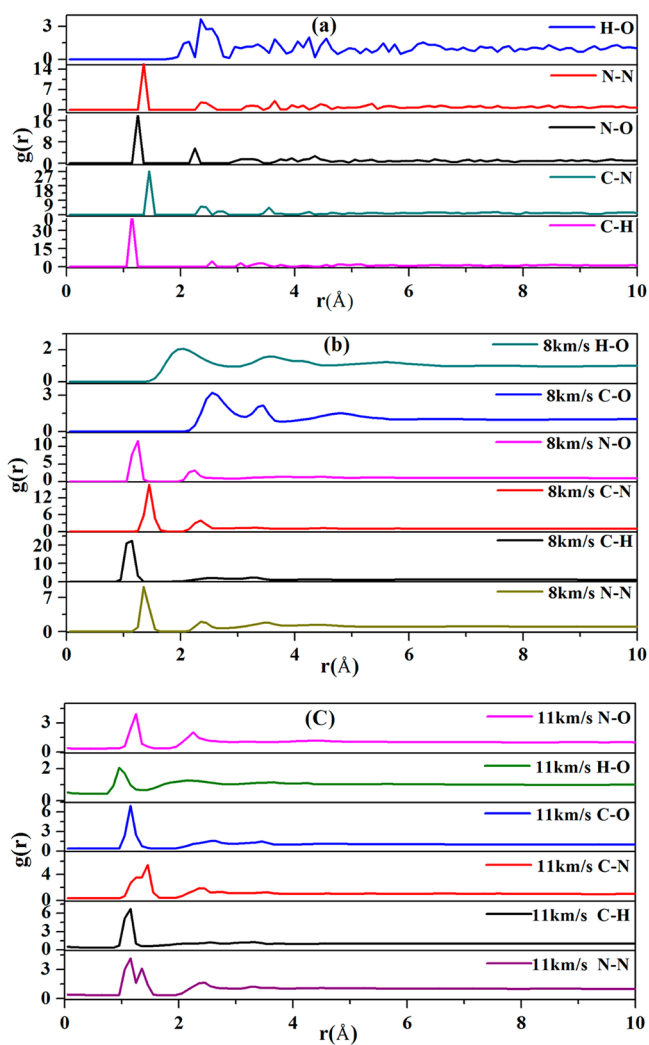


**Figure 5.** Calculated pair radial distribution functions under various impact velocities.

at higher pressure. Our results are consistent with the result of the Brill et al.<sup>5</sup> To date, it was not always possible to guess which pathway will be preferred under the conditions of shock initiation of detonation with high pressures and temperatures, because the nitro compounds undertook very complex reaction pathways to complete explosion.<sup>34b</sup> Recent studies have revealed that the first step is homolysis of the C–H bond. Then other study indicated that the first step is homolysis of the C–N bond and N– $\text{NO}_2$ . In this paper, we proposed an elimination mechanism for the thermolysis of these complex energetic materials under the conditions of the different impact velocities. We found that the first step was homolysis of the N– $\text{NO}_2$  bond at the 8 km/s velocity. When the velocity impact increases to the 11 km/s, we found that the first step was homolysis of the C–H bond.

**3.3. Pair Correlation Functions (PCFs) of HMX with the Different Impact Velocity.** To clarify the structural change of HMX under shock conditions, we calculated the pair correlation functions (PCFs) for each pair of atom types, which give the probability of finding an atom of a given type at a given distance from a reference atom. The PCF for the initial state (before shock compressions) is presented in Figure 5a; moreover, the PCFs for  $V_{\text{imp}} = 8$  km/s and  $V_{\text{imp}} = 11$  km/s are presented in Figure 5b,c, respectively. One sees from Figure 5a,



the peak of C–H, N–N, H–O, N–O, and C–N PCFs  $g_{\text{C-H}}(r)$ ,  $g_{\text{N-N}}(r)$ ,  $g_{\text{H-O}}(r)$ ,  $g_{\text{N-O}}(r)$ , and  $g_{\text{C-N}}(r)$  located around 1.12, 1.33, 2.11 (and 2.13), 1.23, and 1.44 Å, respectively, which are in good accord with 1.14, 1.37, 2.17, 1.23, and 1.45 Å calculated with DFT method by Cui et al.<sup>29</sup>

When the detonation wave passed through the material with  $V_{\text{imp}} = 8$  km/s, the peaks of C–H, C–O, N–N, H–O, N–O, and C–N PCFs  $g_{\text{C-H}}(r)$ ,  $g_{\text{C-O}}(r)$ ,  $g_{\text{N-N}}(r)$ ,  $g_{\text{H-O}}(r)$ ,  $g_{\text{N-O}}(r)$ , and  $g_{\text{C-N}}(r)$  were located around 1.15, 2.54, 1.35, 2.05, 1.25, and 1.45 Å, as shown in Figure 5b, which corresponded to our calculated equilibrium internuclear distance, indicating that HMX molecules kept their original molecular shapes. As previously described, when the impact velocity passed through the material with 8 km/s, there is little chemical reaction. So, the chemical bonds of the HMX molecule were intact.

When the impact velocity increases to 11 km/s, with an increase in the pressure and temperature, the maximum of the PCFs  $g_{\text{C-H}}(r)$ ,  $g_{\text{N-O}}(r)$ , and  $g_{\text{C-N}}(r)$  had a significant reduction, respectively, this indicated that HMX broke up. As the difference between the length of the C–O bond in the CO molecule (1.13 Å) and that of the CO<sub>2</sub> molecule (1.16 Å) is very small, the appearances of their PCFs are similar. From Figure 5c, the peak of C–O PCF  $g_{\text{C-O}}(r)$  had a clear increase around 1.13 Å, the decomposition products of HMX included the mixture of CO and CO<sub>2</sub>. From Figure 5, when the impact velocity increases from 8 to 11 km/s, the maximum for  $g_{\text{H-O}}(r)$  changed from 2.05 to 0.95 Å, which was a typical value of water, such that HMX decomposed to produce H<sub>2</sub>O and H–O. At the same time, the N–N bond length changed to 1.15 Å at 11 km/s, which is close to the value of nitrogen, nitrogen oxide, and nitrous oxide. The above analysis again suggests that decomposition of HMX generates small molecules, N<sub>2</sub>O, N<sub>2</sub>O, and N<sub>2</sub> under the 11 km/s velocity impact.

#### 4. CONCLUSIONS

We have performed molecular dynamics simulations in conjunction with the multiscale shock technique (MSST) to study the initial chemical processes of condensed-phase HMX under shock wave loading. A self-consistent charge density-functional tight-binding (SCC-DFTB) method was used. We find that the decomposition pathway of HMX in the condensed phase is dependent on the shock wave velocity. The N–NO<sub>2</sub> bond dissociation is the primary pathway for HMX decomposition in its early stages for low velocity impact (8 km/s). Then at high velocity impact (10 and 11 km/s), the homolytic cleavage of the N–NO<sub>2</sub> bond is suppressed under high pressure,<sup>15,18</sup> the C–H bond dissociation is the primary pathway for HMX. In an earlier study of RDX, Strachan et al.<sup>64</sup> and Brill et al.<sup>5</sup> reported that C–H bond was easier to fracture under high pressure. In addition, Cui et al.<sup>29</sup> found that the N–NO<sub>2</sub> and C–N of crystal  $\beta$ -HMX were easily compressed with the increasing pressure and, then, became relatively strong and stable. In contrast, the C–H bonds became weak under the high pressure. Our conclusion would be related to the previous theoretical results. This represents the first study of decomposition mechanism of the solid-state structure  $\beta$ -HMX at various impact velocities, which provides new insight into understanding of chemical reactions in wavefront in atomic details.

#### AUTHOR INFORMATION

##### Corresponding Author

\*Tel: +8608162485108. E-mail: G.F.J., cyfjkf@caep.ac.cn; X.R.C., xrchen@scu.edu.cn; D.Q.W., dqwei@sjtu.edu.cn.

#### Notes

The authors declare no competing financial interest.

#### ACKNOWLEDGMENTS

This work is supported by grants from the National Natural Science Foundation of China under Grant No. 11174214 and 11174201, the National Key Laboratory Fund for Shock Wave and Detonation Physics Research of the China Academy of Engineering Physics under Grant No. 9140C671101110C6709, the Defense Industrial Technology Development Program of China under Grant No. B1520110002, the National Basic Research Program of China under Grant Nos. 2010CB731600 and 2011CB808201, and the State Key Laboratory of Explosion Science and Technology, Beijing Institute of Technology, under the contract No. KFJJ12-2Y.

#### REFERENCES

- (1) Zaug, J. M. In *Proceedings of the Eleventh International Detonation Symposium*; Office of Naval Research Press: Snowmass, CO, 1998; pp 498–507.
- (2) Dick, J. J.; Martinez, A. R. *AIP Conf. Proc.* **2002**, 620, 817–820.
- (3) Marsh, S. P. *LASL Shock Hugoniot Data*; University of California Press: Berkeley, CA, 1980.
- (4) Yoo, C.-S.; Cynn, H. *J. Chem. Phys.* **1999**, 111, 10229–10235.
- (5) Brill, T. B.; Brush, P. J. *Philos. Trans. R. Soc.* **1992**, 339, 377–385.
- (6) Brill, T. B.; Arisawa, H.; Brush, P. J.; Gongwer, P. E.; Williams, G. K. *J. Phys. Chem.* **1995**, 99, 1384–1392.
- (7) Tang, C. J.; Lee, Y. J.; Kudva, G.; Litzinger, T. A. *Combust. Flame* **1999**, 117, 170–188.
- (8) Pulham, C. R.; Millar, D. I. A.; Oswald, I. D. H.; Marshall, W. G. *High-Pressure Crystallography: From Fundamental Phenomena to Technological Applications—NATO Science for Peace and Security Series B: Physics and Biophysics*; Springer, New York, 2010; pp 447–457.
- (9) Engelke, R.; Blais, N. C.; Sheffield, S. A. *J. Phys. Chem. A* **2010**, 114, 8234–8239.
- (10) Zoh, K. D.; Stenstrom, M. K. *Water Res.* **2002**, 36, 1331–1341.
- (11) Sewell, T. D.; Menikoff, R.; Bedrov, D.; Smith, G. D. *J. Chem. Phys.* **2003**, 119, 7417–7426.
- (12) Boldyreva, E.; Dera, P. *High-Pressure Crystallography: From Fundamental Phenomena to Technological Applications—NATO Science for Peace and Security Series B: Physics and Biophysics*; Springer, New York, 2010; pp 183–192.
- (13) Van der Heijden, A. E. D. M.; Bouma, R. H. B. *Cryst. Growth Des.* **2004**, 4, 999–1007.
- (14) Zhang, S. W.; Truong, T. N. *J. Phys. Chem. A* **2000**, 104, 7304–7307.
- (15) Zhang, S. W.; Truong, T. N. *J. Phys. Chem. A* **2001**, 105, 2427–2434.
- (16) Lewis, J. P.; Glaesemann, K. R.; Vanopdorp, K.; Voth, G. A. *J. Phys. Chem. A* **2000**, 104, 11384–11389.
- (17) Sharia, O.; Kuklja, M. M. *J. Phys. Chem. B* **2011**, 115, 12677–12686.
- (18) Wang, J.; Brower, K. R.; Naud, D. L. *J. Org. Chem.* **1997**, 62, 9055–9060.
- (19) Sharia, O.; Kuklja, M. M. *J. Am. Chem. Soc.* **2012**, 134, 11815–11820.
- (20) Sharia, O.; Kuklja, M. M. *J. Phys. Chem. C* **2012**, 116, 11077–11081.
- (21) Glascoe, E. A.; Hsu, P. C.; Springer, H. K.; Dehaven, M. R.; Tan, N.; Turner, H. C. *Thermochim. Acta* **2011**, 515, 58–66.
- (22) Henson, B. F.; Smilowitz, L.; Asay, B. W.; Dickson, P. M. *J. Chem. Phys.* **2002**, 117, 3780–3788.
- (23) Brill, T. B.; Karpowicz, R. J. *J. Phys. Chem.* **1982**, 86, 4260–4265.
- (24) Ji, G. F.; Xiao, H. M.; Dong, H. S. *Acta Chim. Sin.* **2002**, 60, 194–199.
- (25) Prasad, K.; Yetter, R. A.; Smooke, M. D. *Combust. Flame* **1998**, 115, 406–416.



- (26) Suryanarayana, B.; Graybush, R. J.; Autera, J. R. *Chemistry and Industry* **1967**, 52, 2177–2178.
- (27) McGuire, R. R.; Tarver, C. M. In *Proceedings of Seventh Symposium (International) on Detonation*; Naval Surface Weapons Center Press: Annapolis, Maryland, 1981; pp 56–65.
- (28) Zhu, W. H.; Huang, H.; Huang, H. J. *J. Chem. Phys.* **2012**, 136, 044516–044516-6.
- (29) Cui, H. L.; Ji, G. F.; Chen, X. R.; Zhu, W. H.; Wei, D. Q. *J. Phys. Chem. A* **2010**, 114, 1082–1092.
- (30) Lewis, J. P. *Chem. Phys. Lett.* **2003**, 371, 588–593.
- (31) The CP2K developers group, <http://cp2k.berlios.de/>, 2007.
- (32) Reed, E. J.; Fried, L. E.; Joannopoulos, J. D. *Phys. Rev. Lett.* **2003**, 90, 235503–235503-4.
- (33) Kadau, K.; Germann, T. C.; Lomdahl, P. S.; Holian, B. L. *Science* **2002**, 296, 1681–1684.
- (34) (a) Goldman, N.; Reed, E. J.; Kuo, I.-F.; Fried, L. E.; Mundy, C. J.; Curioni, A. J. *Chem. Phys.* **2009**, 130, 124517–124517-6. (b) Reed, E. J.; Manaa, M. R.; Fried, L. E.; Glaesemann, K. R.; Joannopoulos, J. D. *Nat. Phys.* **2008**, 4, 72–76.
- (35) Chang, J.; Lian, P.; Wei, D. Q.; Chen, X. R.; Gong, Z. Z.; Zhang, Q. M. *Phys. Rev. Lett.* **2010**, 105, 188302–188305.
- (36) Mundy, C. J.; Curioni, A.; Goldman, N.; Kuo, I. F. W.; Reed, E. J.; Fried, L. E.; Ianuzzi, M. J. *Chem. Phys.* **2008**, 128, 184701–184701-6.
- (37) Manaa, M. R.; Reed, E. J.; Fried, L. E.; Goldman, N. J. *Am. Chem. Soc.* **2009**, 131, 5483–5487.
- (38) Elstner, M.; Porezag, D.; Jungnickel, G.; Elsner, J.; Haugk, M.; Frauenheim, Th.; Suhai, S.; Seifert, G. *Phys. Rev. B* **1998**, 58, 7260–7268.
- (39) Elstner, M.; Hobza, P.; Frauenheim, T.; Suhai, S.; Kaxiras, E. J. *Chem. Phys.* **2001**, 114, 5149–5155.
- (40) Cui, Q.; Elstner, M.; Kaxiras, E.; Frauenheim, T.; Karplus, M. J. *Phys. Chem. B* **2001**, 105, 569–585.
- (41) Manaa, M. R.; Fried, L. E.; Melius, C. F.; Elstner, M.; Frauenheim, T. J. *Phys. Chem. A* **2002**, 106, 9024–9029.
- (42) Margetis, D.; Kaxiras, E.; Elstner, M.; Frauenheim, Th; Manaa, M. R. *J. Chem. Phys.* **2002**, 117, 788–799.
- (43) Reed, E. J.; Joannopoulos, J. D.; Fried, L. E. *Phys. Rev. B* **2000**, 62, 16500–16509.
- (44) Cady, H. H.; Larson, A. C.; Kromer, D. T. *Acta Crystallogr.* **1963**, 16, 617–623.
- (45) Choi, C. S.; Boutin, H. P. *Acta Crystallogr.* **1970**, B26, 1235–1240.
- (46) Eiland, P. R.; Pepinsky, R. Z. *Kristallogr.* **1955**, 106, 273–298.
- (47) (a) Zerilli, F. J.; Kuklja, M. M. *J. Phys. Chem. A* **2006**, 110, 5173–5179. (b) Zerilli, F. J.; Kuklja, M. M. *J. Phys. Chem. A* **2010**, 114, 5372–5376.
- (48) Conroy, M. W.; Oleynik, I. I.; Zybin, S. V.; White, C. T. *J. Appl. Phys.* **2008**, 104, 053506–053506-6.
- (49) Cui, H. L.; Ji, G. F.; Zhao, J. J.; Zhao, F.; Chen, X. R.; Zhang, Q. M.; Wei, D. Q. *Mol. Simul.* **2010**, 36, 670–681.
- (50) Olinger, B.; Roof, B.; Cady, H. *Proceedings of Du Symposium International sur le Comportement des Milieux Denses Sous Hautes Pressions Dynamiques*; ed.s du Commissariat al'Energie Atomique; Centre d'Etudes Nucleaires de Sarclay: Paris, 1978; pp 3–8.
- (51) Yoo, C. S.; Akella, J.; Cynn, H.; Nicol, M. F. *Phys. Rev. B* **1997**, 56, 140–146.
- (52) Gump, J. C.; Peiris, S. M. *J. Appl. Phys.* **2005**, 97, 053513–053513-7.
- (53) Zhang, L. Z.; Zybin, S. V.; van Duin, A. C. T.; Dasgupta, S.; Goddard, W. A, III; Kober, E. M. *J. Phys. Chem. A* **2009**, 113, 10619–10640.
- (54) Lyman, J. L.; Liau, Y. C.; Brand, H. V. *Combust. Flame* **2002**, 130, 185–203.
- (55) Melius, C. F. In *Chemistry and Physics of Energetic Materials*; Bulusu, S. N., Ed.; Kluwer Academic Press: Dordrecht, The Netherlands, 1990; pp 21–49.
- (56) Melius, C. F. In *Chemistry and Physics of Energetic Materials*; Bulusu, S. N., Ed.; Kluwer Academic Press: Dordrecht, The Netherlands, 1990; pp 51–78.
- (57) Tarver, C. M.; Tran, T. D. *Combust. Flame* **2004**, 137, 50–62.
- (58) Prasad, K.; Yetter, R. A.; Smooke, M. D. *Combust. Flame* **1998**, 115, 406–416.
- (59) Chakraborty, D.; Muller, R. P.; Dasgupta, S.; Goddard, W. A, III. *J. Phys. Chem. A* **2001**, 105, 1302–1314.
- (60) Tarver, C. M. *J. Phys. Chem. A* **1997**, 101, 4845–4851.
- (61) Guo, Y. Q.; Greenfield, M.; Bernstein, E. R. *J. Chem. Phys.* **2005**, 122, 244310–244310-6.
- (62) Im, H.-S.; Bernstein, E. R. *J. Chem. Phys.* **2000**, 113, 7911–7918.
- (63) Im, H.-S.; Bernstein, E. R. *J. Phys. Chem. A* **2002**, 106, 7565–7572.
- (64) Strachan, A.; van Duin, A. C. T.; Chakraborty, D.; Dasgupta, S.; Goddard, W. A, III. *Phys. Rev. Lett.* **2003**, 91, 09301–098301-4.
- (65) Patterson, J. E.; Dreger, Z. A.; Miao, M. S. J. *Phys. Chem. A* **2008**, 112, 7374–7382.
- (66) Manaa, M. R.; Reed, E. J.; Fried, L. E.; Galli, G.; Gygi, F. J. *Chem. Phys.* **2004**, 120, 10146–10153.